TURBULENT TRANSPORT OF MASS AND MOMENTUM IN OPEN-CHANNEL FLOW OVER A HETEROGENEOUS PARTICLE BED

Sourabh V Apte
School of Mechanical, Industrial, and Manufacturing Engineering
Oregon State University
204 Rogers Hall,
Corvallis, OR 97331
email: sva@oregonstate.edu

Phurin Nilket
School of Mechanical, Industrial, and Manufacturing Engineering
204 Rogers Hall,
Corvallis, OR 97331
email: nilketp@oregonstate.edu

ABSTRACT

Pore-resolved direct numerical simulations (PR-DNS) are performed in a doubly periodic open channel configuration to investigate mass and momentum transport of turbulent flow over a porous bed of randomly packed spherical particles. Two permeability Reynolds numbers, $Re_K \in [2.56, 5.17]$ corresponding to friction Reynolds numbers, $Re_\tau \in [270, 540]$ and representative of natural stream flows are simulated over a bed of mono- and polydispersed particles of same mean diameter $D_{p,50}$ and porosity of 0.418. Passive scalar transport at unity Schmidt number is computed with prescribed scalar concentrations at the top and bottom boundaries. Turbulent shear and bed-normal stresses increase with Re_K and peak near the interface, whereas the form-induced dispersive stresses and dispersive scalar transport peak inside the top layer of the bed and show little difference between the polydispersed and monodispersed beds. The turbulent diffusivity dominates scalar mixing in the free flow and near the interface. For higher Re_K, pockets of turbulent fluctuations penetrate deeper into the bed and cause dispersive scalar transport that peaks and remains significant deeper inside the bed and is slightly higher for the polydispersed case.

INTRODUCTION

Interchange of mass and momentum between surface water and ground water occurs in the porous bed beneath the streams, termed as the hyporheic zone. The exchange of mass and momentum (hyporheic exchange) of solutes such as chemicals and pollutants, dissolved oxygen, nutrients, and heat across this zone is a critical component in sustaining diverse aquatic ecosystems. The penetration of mean and turbulent flow within the porous bed and near bed pressure fluctuations have been identified (Hester *et al.*, 2017) to play a crucial in understanding this hyporheic exchange. While there are many parameters which characterize exchange of mass and momentum across the sediment water interface (SWI), the permeability Reynolds number, representing the ratio between the permeability scale to the viscous scale $\sqrt{K}/(\nu/u_\tau)$, is typically used to identify different flow regimes based on the dominant transport mechanisms across the SWI. Based on the characterization by Voermans *et al.* (2017); Grant *et al.* (2018) turbulence is dominant near the SWI for $Re_K > 1$ (see figure 1).

Recent pore-resolved DNS simulations by Apte and coworkers (Karra *et al.*, 2023, 2025), quantified the differences in turbulence structure and pressure fluctuations between randomly packed sediment bed made of monodispered spherical particles and rough impermeable walls with roughness characteristics derived from the top layer of the particles. It was found that turbulence structures in the free stream and pressure fluctuations at the sediment-water interface (SWI) are better captured by considering at least the top layer of sediment bed for lower Re_K numbers. Influence of varying Re_K (with values $(1 < Re_K < 10)$ found in typical aquatic beds) on turbulent flow statistics near the SWI was also investigated in detail. Wenczowski & Manhart (2025) used PR-DNS data on passive scalar transport in similar configurations for $Re_K \sim 0.4 - 2.8$ to quantify the contributions of turbulent, dispersive, and diffusive mass transport mechanisms. They showed that in the free flow region turbulent scalar transport dominates, whereas, dispersive transport and molecular diffusion gain importance near the interface, and the normalized effective diffusivity scales as Re_K^2. Sarwar *et al.* (2024) conducted PR-DNS studies on momentum transport across the sediment-water interface at friction Reynolds number of $Re_\tau = 300$ with heterogeneous, polydispersed distribution of spherical particles with a focus on quantifying the drag force variation on the particles.

The present study aims at extending these recent simulations at lower Reynolds numbers to higher Reynolds numbers with focus on both mass and momentum transport. Specifically, PR-DNS data are used to compare transport mechanisms across the sediment-water interface for two Reynolds numbers ($Re_K = 2.56$ and $Re_K = 5.1$) for mono and polydispersed beds of spherical particles with same mean diameter and porosity. Distribution of particle sizes is chosen based on typical variation observed in nature and data collected at local a creek (Jackson *et al.*, 2013). The goal is to also provide insights and quantifiable data on pressure and turbulent kinetic energy distributions at the interface, drag force variations within the bed, and effective diffusivity at the interface to help improve reduced-order models and correlations.

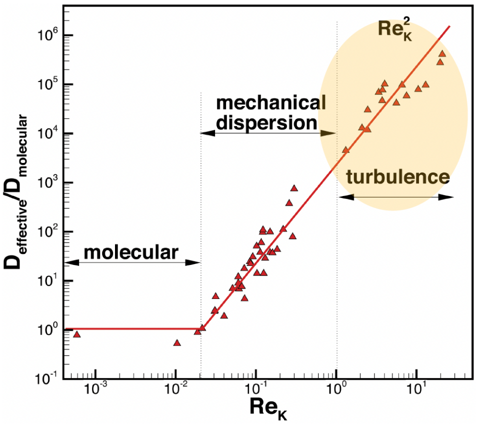

Figure 1. Effective dispersion coefficient versus Re_k (based on Voermans *et al.* (2017); Grant *et al.* (2018)).

SIMULATION SETUP

The computational domain for the permeable sediment bed used in this study consists of a doubly periodic (x and z) domain with four layers of randomly packed, spherical sediment grains at the bottom to capture the turbulence penetration and unsteady, inertial flow (figure 2a). Random packing of mono– and poly–dispersed spherical particles is generated such that any particle surface crossing the periodic boundaries are cut and transferred to enforced periodicity using the code developed by Dye *et al.* (2013) which applies the collective rearrangement algorithm introduced by Williams & Philipse (2003), coupled with a mechanism for controlling the system overall porosity. In order to have direct comparison between the mono and polydispersed beds, the averaged particle size ($D_{p,50}$) and the bed porosity are kept the same.

Flow and Particle Parameters

Turbulent flow over a permeable bed can be characterized by the permeability Reynolds number (Re_K), the turbulent Reynolds number (Re_τ), the ratio of sediment depth (H_s) to the free-surface height (δ), the ratio of the mean sediment grain diameter to the free-surface height ($D_{p,50}/\delta$), bed porosity which is held constant ($\theta = 0.418$), and the domain lengths in the axial and spanwise directions normalized by the free-surface height (L_x/δ, L_z/δ). PDF of polydispersed particle size distribution is shown in figure 2b. Both monodispersed and polydispersed particle beds that yield roughly the same mean diameter D_{50} and porosity (figure 2c) are investigated. The polydispersed particle size distribution (figure 2b) is based on realistic size variations observed in natural streams (Jackson *et al.*, 2013). Two Reynolds numbers (see Table 1) in the turbulent regime, $Re_K = 2.56$ (PBL) and $Re_K = 5.1$ (PBH) are simulated with unit Schmidt number for passive scalar.

Numerical Method and Boundary Conditions

The numerical approach is based on a fictitious domain method to handle arbitrary shaped immersed objects without requiring the need for body-fitted grids (Apte *et al.*, 2009). The following governing equations are solved over the entire domain, including the region within the solid bed, and a rigidity constraint force, $\mathbf{f}$, is applied that is non-zero only in the solid region. The governing equations are given as:

Table 1. Simulation parameters: $D_{p,50}$, $D_{p,\min}$ and $D_{p,\max}$ are the mean, minimum, and maximum diameters, δ is the flow height, H_s is sediment depth, and $\theta = 0.418$ is porosity.

	PBL	PBH
Re_K, Re_τ	2.56, 270	5.17, 540
H_s/δ	1.14	1.14
$D_{p,50}/\delta$	0.29	0.29
$D_{p,\min}/\delta$, $D_{p,\max}/\delta$	0.212, 0.384	0.212, 0.384
$(L_x, L_z)/\delta$	$(4\pi, 2\pi)$	$(2\pi, \pi)$

$$\nabla \cdot \mathbf{u} = 0, \tag{1}$$

$$\rho \left[\frac{\partial \mathbf{u}}{\partial t} + (\mathbf{u} \cdot \nabla)\mathbf{u} \right] = -\nabla p + \mu \nabla^2 \mathbf{u} + \mathbf{f} \tag{2}$$

where $\mathbf{u}$ is the velocity vector (with components given by $\mathbf{u} = (u_x, u_y, u_z)$, ρ is the fluid density, μ the fluid dynamic viscosity, and p the pressure. A fully parallel, structured, collocated grid solver has been developed and thoroughly verified and validated for a range of test cases including flow over a cylinder and sphere for different Reynolds numbers, flow over touching spheres at different orientations, flow developed by an oscillating cylinder, among others. The details of the algorithm as well as very detailed verification and validation studies have been published (Apte *et al.*, 2009; Finn & Apte, 2013).

Cartesian grids are used in the entire simulation domain, including both fluid and solid phases. An additional body force is imposed on the solid part to enforce the rigidity constraint and satisfy the no-slip boundary condition. Transport of a passive scalar is simulated by solving,

$$\frac{\partial(\psi c)}{\partial t} + \nabla \cdot (\mathbf{u} \psi c) = \nabla \cdot (\psi \Gamma \nabla c), \tag{3}$$

where Γ is the scalar diffusivity, ψ represents the color function (or fluid volume fraction) which is 0 within the solid, $\psi = 1$ within the fluid, whereas $0 < \psi < 1$ represents the diffuse interface of the particle boundary. The passive scalar advection is solved by third-order WENO scheme. No penetration (zero gradient) Neumann condition on particle surfaces is imposed so that there is no leakage of the scalar into the solid boundary,

$$\nabla c \cdot \hat{\mathbf{n}} \equiv \nabla c \cdot \left(\frac{\nabla \psi}{|\nabla \psi|} \right) = 0, \tag{4}$$

where $\hat{\mathbf{n}}$ is the outward normal at the particle surface. The above boundary condition on the particle surface is combined with the scalar transport equation to impose the no penetration boundary condition following the algorithm developed by Berry *et al.* (2013) resulting in the scalar transport equation (3). Slip conditions are used for velocity at the top and bottom surfaces. Dirichlet conditions of $c_t = 1$ (top) and $c_b = 0$ (bottom) are applied for the passive scalar. These conditions result in constant value of plane-averaged *net* scalar flux at any y location.

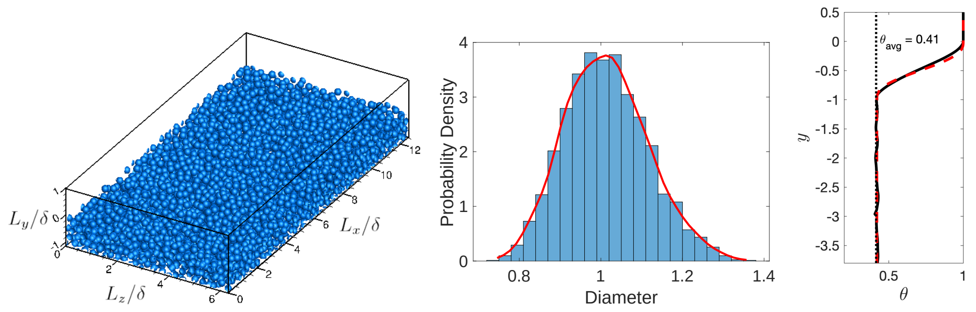

(a) (b) (c)

Figure 2. (a) Permeable bed and doubly periodic (x and z directions) computational domain, (b) pdf of particle size distribution for the polydispersed bed, and (c) bed-normal porosity variation.

The grid resolutions required for these configurations are based on two main considerations: (i) minimum bed-normal grid resolution near the bed, and (ii) minimum resolution required to capture flow over spherical particles. For DNS of boundary layers, the bed-normal grid resolution in wall units should be $\Delta y^+ < 1$, in order to accurately capture the bed shear stress in the turbulent flow. The grid resolutions in the axial and spanwise directions are typically 3–4 times coarser following the smooth channel flow simulations by Moser *et al.* (1999). Note that, the roughness features and permeability are known to break the elongated flow structures along the axial direction in smooth walls, reducing the inhomogeneity in the near-bed region and alleviating the bed-normal grid resolution requirement near the bed. Accordingly, roughly 180 grid points for the PBL case and 308 points for the PBH case are used in the bed-normal direction *within each sediment particle based on the smallest particle diameter* in the top two layers. In the x and z directions, uniform grid with 26 and 38 grid points are used per smallest particle diameter to resolve the grain geometry for the PBL and PBH cases, respectively. This results in $\Delta x^+ = \Delta z^+ = 3.01, 4.06$ for PBL and PBH cases with $\Delta y^+ = 0.95$ for both. A fully parallel, structured, collocated grid solver that is validated against experimental data (Voermans *et al.*, 2017) for turbulent flows over porous particle bed is used (Karra *et al.*, 2023, 2025).

RESULTS

In this section, the DNS data is first validated against the experimental data of Voermans *et al.* (2017) followed by results for passive scalar transport for different Reynolds numbers and particle configurations.

Comparison with experimental data

Since the flow properties are highly spatially heterogeneous near rough sediments, double averaging procedure (Raupach & Thom, 1981) is used, wherein spatial averaging is performed along with time averaging,

$$\phi(x,t) = \langle\overline{\phi}\rangle(y) + \widetilde{\phi}(x) + \phi'(x,t) \qquad (5)$$

where ϕ is an instantaneous flow variable, $\langle\phi\rangle$ is the intrinsic spatial average in the (x,z) plane, $\langle\phi\rangle = 1/A_f \int_{A_f} \phi dA$ (where A_f is the area occupied by the fluid), $\overline{\phi}$ is the temporal average, $\phi' = \phi - \overline{\phi}$ is the instantaneous turbulent fluctuation and $\widetilde{\phi} = \overline{\phi} - \langle\overline{\phi}\rangle$ is the form-induced or dispersive fluctuation. Accordingly, Reynolds stresses and form-induced stresses shown in this section are computed using the double averaging procedure.

Pore-resolved direct numerical simulations of turbulent boundary layer flow over a sediment bed were first validated with experimental data from Voermans *et al.* (2017). Permeable bed case with porosity of 0.41, $Re_K = 2.56$ and $Re_\tau \sim 180$ matches with Case L12 in Voermans *et al.* (2017), which is within the range for realistic aquatic sediments beds. Although the averaged bed porosity is same in both studies, the approach applied to generate the randomly packed sediment particle bed is different.

The double-averaged (DA) mean velocity profile normalized by free-surface velocity U_δ is shown in figure 3a. Excellent agreement is seen between the DNS data and experimental measurements. Figures 3b, and 3c, show a comparison of DA turbulence intensities, namely stream-wise, and wall normal stresses. Again very good agreement between DNS and experiment is observed. The form-induced intensities or dispersive stresses normalized by u_τ are shown in figures 3d, and 3e. Upon initial observation, noticeable differences are observed between current DNS and experimental results for dispersive stresses which can be explained as follows. Firstly, as mentioned in the previous section, spatial averaging is carried out over an entire $x-z$ plane at a given y location for DNS results. While for the experimental data, spatial averaging was performed over three different spanwise locations over six different measurements. To quantify the differences in the sampling procedures between the experiments and DNS, the experimental sampling process is replicated in the DNS data whereby spatial averaging is carried out at a few finite uncorrelated spanwise locations and repeated over different streamwise locations. A family of curves, shown by grey squares, indicates the associated uncertainty in the processing of the experimental data. The averaged experimental and DNS data are within this scatter for all axial locations. Secondly, it is has been reported in literature Nikora *et al.* (2002); Fang *et al.* (2018) that the spanwise averaging is highly sensitive to the geometry at the sediment-water interface. For the present DNS, only the mean porosity of the randomly distributed arrangement of mono-dispersed spherical particles is matched with the experimental geometry. However, the exact sediment-grain distribution in the experiments is unknown and is likely different compared to that used in DNS. This difference, especially near the top of the bed can also contribute to differences in the form-induced or dispersive stresses.

Figures 4a-c show the bed-normal variation of the double-averaged normalized axial and bed-normal turbulence intensities as well as the normalized drag force per unit volume for the mono and polydispersed cases at both Reynolds numbers. It is

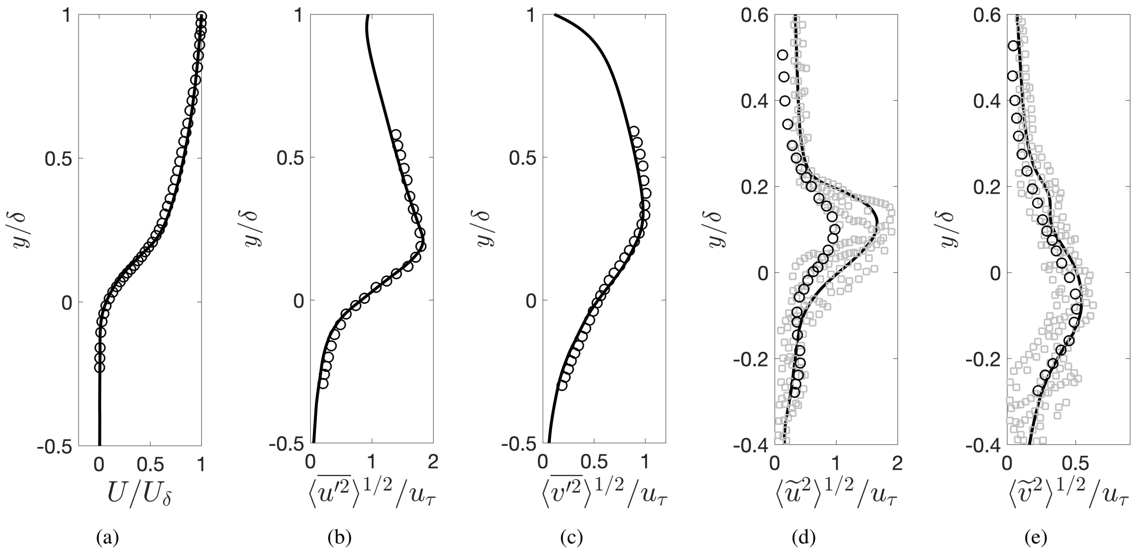

Figure 3. Comparison of (a) mean velocity and (b) streamwise, and (c) wall-normal components of Reynolds stress tensor, (d) streamwise and (e) wall-normal components of form-induced stress tensor for monodispersed case at $Re_K = 2.56$. Experimental data by Voermans *et al.* (2017) (○), emulating experimental sampling (□), PR-DNS (—). For these plots, the origin is the inflection point in the porosity profile ($\partial_{yy}\theta = 0$) following the way the experimental data is presented.

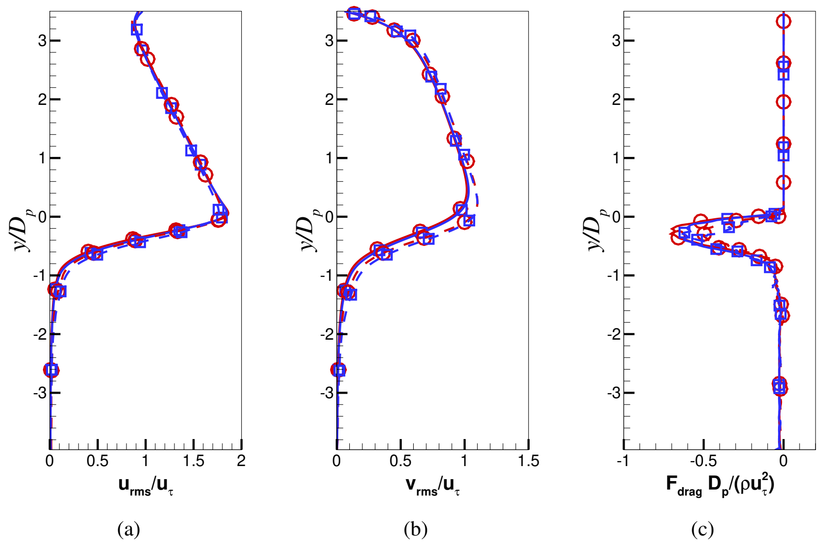

Figure 4. Bed-normal variation of (a) normalized axial rms velocity, (b) normalized vertical rms velocity, and (c) normalized drag force per unit volume for (i) $Re_K = 2.56$ monodispersed (—○—) and polydispersed (—□—), (ii) $Re_K = 5.1$ monodispersed (- -○- -) and polydispersed (- -□- -).

found that the particle bed configuration does not significantly affect these statistics for the present random arrangement with same mean diameter and porosity. The turbulence intensities and the drag force are higher for higher Reynolds numbers, but when normalized by the friction velocity, all data collapse.

Passive scalar transport

Instantaneous contours of normalized passive scalar concentration in the center-plane for the two Reynolds numbers are shown for the polydispersed bed in figure 5. Turbulent mixing dominates in the free flow providing nearly uniform concentrations. Sweep and ejection events near the interface and resultant pressure fluctuations cause advective pumping effect resulting localized deeper penetration of scalar concentration within the bed. Strong scalar concentration gradients prevail within the sediment bed. The interaction between turbulent fluid motion and the scalar concentration field is visible near the interface suggesting enhanced turbulent mixing at these locations.

Figure 6a shows the double-averaged, bed-normal variation of the mean scalar concentration for the mono and polydispersed cases at low and high Re_K. The mean scalar concentration is similar for all cases. The superficially averaged net

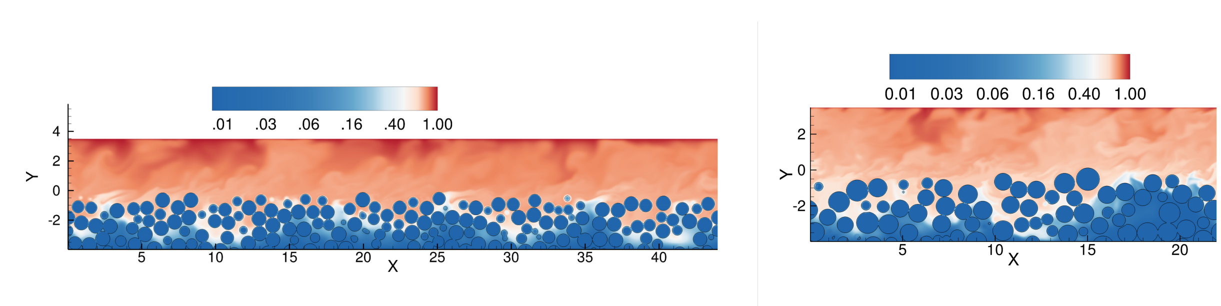

(a) (b)

Figure 5. Instantaneous contours of passive scalar ($(c-c_{\mathrm{b}})/(c_{\mathrm{t}}-c_{\mathrm{b}})$) in the center-plane for the polydispersed bed: (a) $Re_K = 2.56$, (b) $Re_K = 5.1$).

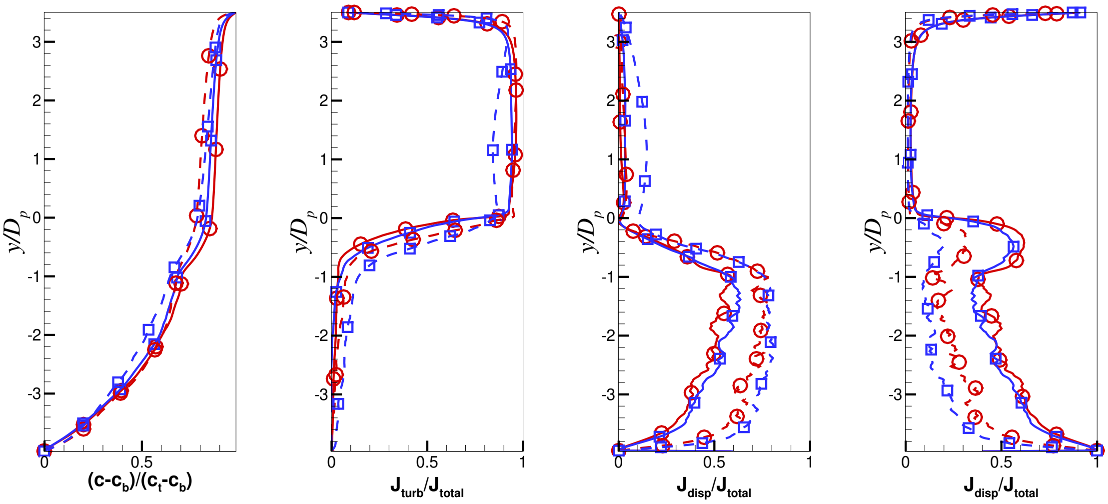

(a) (b) (c) (d)

Figure 6. Bed-normal variation of (a) mean concentration, (b) normalized turbulent scalar flux, and (c) normalized dispersive scalar flux, and (d) normalized diffusive scalar flux for (i) $Re_K = 2.56$ monodispersed (—○—) and polydispersed (—□—), (ii) $Re_K = 5.1$ monodispersed (- -○- -) and polydispersed (- -□- -).

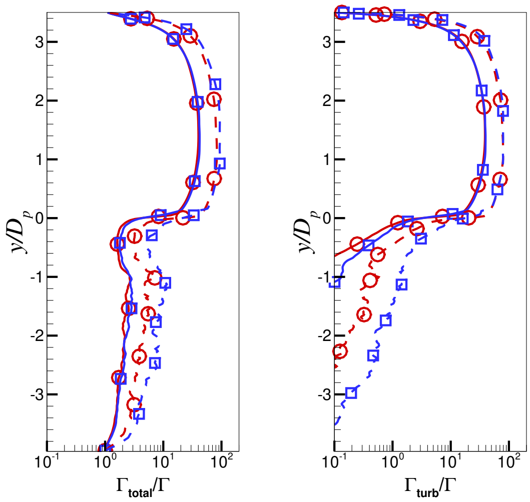

(a) (b)

Figure 7. Bed-normal variation of effective (a) normalized total diffusivity, and (b) normalized turbulent diffusivity for (i) $Re_K = 2.56$ monodispersed (—○—) and polydispersed (—□—), (ii) $Re_K = 5.1$ monodispersed (- -○- -) and polydispersed (- -□- -).

total scalar flux at any y location is given as,

$$\begin{aligned} J_{\text{total}} &= J_{\text{turbulent}} + J_{\text{dispersive}} + J_{\text{diffusive}} \\ &= \underbrace{\theta \left\langle \overline{c'v'} \right\rangle}_{\text{turbulent}} + \underbrace{\theta \left\langle \tilde{\bar{c}}\, \tilde{\bar{v}} \right\rangle}_{\text{dispersive}} - \underbrace{\theta \left\langle \Gamma \frac{d\bar{c}}{dy} \right\rangle}_{\text{diffusive}}. \end{aligned} \quad (6)$$

The bed-normal distribution of normalized turbulent, dispersive, and diffusive scalar fluxes are plotted in figures 6b-c, respectively. In the freestream, the net flux is dominated by the turbulent flux with diffusive fluxes becoming important only near the top boundary. At the interface the turbulent fluxes are slightly larger for the polydispersed case than the corresponding monodispersed case and maybe attributed to locally larger pockets present in polydispersed beds. The turbulent fluctuations penetrate more than a particle diameter for the higher Re_K case. The dispersive fluxes are dominant within the bed and increase with increasing Reynolds number. However, polydispersity seems to have negligible effect on their magnitudes within the bed. Finally, the diffusive fluxes are also dominant deep within the bed, where the gradients in mean scalar concentration become large. The polydispersed bed shows slightly lower diffusive fluxes compared to the monodispersed particles. Both dispersive and turbulent fluxes are important in the interface region.

Figure 7a,b shows the normalized total and turbulent effective diffusivities obtained as,

$$\frac{\Gamma_{\text{total}}}{\Gamma} = \frac{J_{\text{total}}}{J_{\text{diffusive}}}, \quad \frac{\Gamma_{\text{turb}}}{\Gamma} = \frac{J_{\text{turb}}}{J_{\text{diffusive}}}. \quad (7)$$

The total diffusivity is higher for the higher Re_K, but polydispersity has minimal effect on its distribution. The turbulent diffusivity shows small non-zero values deep within the bed for higher Re_K and polydisperse bed. However, majority of the total diffusivity within the bed comes from the dispersive fluxes which peak at almost 10 times the diffusive fluxes for higher Re_K. The peak occurs below the top layer of particles suggesting of transfer from turbulent fluctuations to form induced variations.

SUMMARY

Effect of polydispersity and flow Reynolds number on mass and momentum transport of turbulent flow over a porous bed of spherical particles is investigated. Pore-resolved direct numerical simulations (PR-DNS) are performed in a doubly periodic open channel configuration. Two permeability Reynolds numbers, $Re_K \in [2.56, 5.17]$ corresponding to friction Reynolds numbers, $Re_\tau \in [270, 540]$ and representative of natural stream flows are simulated over a bed of mono- and polydispersed particles of same mean diameter $D_{p,50}$ and porosity of 0.418. Passive scalar transport at unity Schmidt number is computed with prescribed scalar concentrations at the top and bottom boundaries. Turbulent shear and bed-normal stresses increase with Re_K and peak near the interface, whereas the form-induced dispersive stresses and dispersive scalar transport peak within the bed for both the polydispersed and monodispersed beds. The turbulent diffusivity dominates scalar mixing in the free flow and near the interface. For higher Re_K, pockets of turbulent fluctuations penetrate deeper into the bed and cause dispersive scalar transport that peaks and remains significant deeper inside the bed and is slightly higher for the polydispersed case.

REFERENCES

Apte, S. V., Martin, M. & Patankar, N. A. 2009 A numerical method for fully resolved simulation (FRS) of rigid particle-flow interactions in complex flows. *Journal of Computational Physics* **228** (8), 2712–2738.

Berry, JD, Davidson, Malcolm R & Harvie, DALTON JE 2013 A multiphase electrokinetic flow model for electrolytes with liquid/liquid interfaces. *Journal of Computational Physics* **251**, 209–222.

Dye, Amanda L, McClure, James E, Miller, Cass T & Gray, William G 2013 Description of non-darcy flows in porous medium systems. *Physical Review E* **87** (3), 033012.

Fang, Hongwei, Xu, Han, He, Guojian & Dey, Subhasish 2018 Influence of permeable beds on hydraulically macro-rough flow. *Journal of Fluid Mechanics* **847**, 552–590.

Finn, Justin & Apte, Sourabh V 2013 Relative performance of body fitted and fictitious domain simulations of flow through fixed packed beds of spheres. *International journal of multiphase flow* **56**, 54–71.

Grant, Stanley B., Gomez-Velez, Jesus D. & Ghisalberti, Marco 2018 Modeling the effects of turbulence on hyporheic exchange and local-to-global nutrient processing in streams. *Water Resources Research* **54** (9), 5883–5889.

Hester, Erich T, Cardenas, M Bayani, Haggerty, Roy & Apte, Sourabh V 2017 The importance and challenge of hyporheic mixing. *Water Resources Research* **53** (5), 3565–3575.

Jackson, TR, Haggerty, R & Apte, SV 2013 A fluid-mechanics based classification scheme for surface transient storage in riverine environments: quantitatively separating surface from hyporheic transient storage. *Hydrol. Earth Syst. Sci* **17**, 2747–2779.

Karra, Shashank K, Apte, Sourabh V, He, Xiaoliang & Scheibe, Timothy D 2023 Pore-resolved investigation of turbulent open channel flow over a randomly packed permeable sediment bed. *Journal of Fluid Mechanics* **971**, A23.

Karra, Shashank K, Apte, Sourabh V, He, Xiaoliang, Scheibe, Timothy D & Wood, Brian D 2025 Characteristics of turbulent transport over permeable and impermeable bed of particles. *Transport in Porous Media* **152** (11), 1–27.

Moser, Robert D, Kim, John & Mansour, Nagi N 1999 Direct numerical simulation of turbulent channel flow up to re τ= 590. *Physics of fluids* **11** (4), 943–945.

Nikora, Vladimir Ivanovich, Koll, K, McLean, SR, Ditrich, A & Aberle, J 2002 Zero-plane displacement for rough-bed open-channel flows. In *Fluvial Hydraulics River Flow 2002*, pp. 83–92.

Raupach, MR & Thom, A St 1981 Turbulence in and above plant canopies. *Annual Review of Fluid Mechanics* **13** (1), 97–129.

Sarwar, S, Akiki, G, Balachandar, S, Sleigh, PA & Wright, NG 2024 Direct numerical simulation of open-channel flow over a heterogeneous particle bed at low relative submergence. *Physics of Fluids* **36** (8).

Voermans, JJ, Ghisalberti, M & Ivey, GN 2017 The variation of flow and turbulence across the sediment–water interface. *Journal of Fluid Mechanics* **824**, 413–437.

Wenczowski, S v & Manhart, M 2025 Scalar transport across the interface between a random sphere pack and a turbulent flow. *Journal of Fluid Mechanics* **1012**, A4.

Williams, SR & Philipse, AP 2003 Random packings of spheres and spherocylinders simulated by mechanical contraction. *Physical Review E* **67** (5), 051301.